An Amorphous Phase Precedes Crystallization: Unraveling the Colloidal Synthesis of Zirconium Oxide Nanocrystals

Rohan Pokratath, Laurent Lermusiaux, Stefano Checchia, Jikson Pulparayil Mathew, Susan Rudd Cooper, Jette Katja Mathiesen, Guillaume Landaburu, Soham Banerjee, Songsheng Tao, Nico Reichholf, et al.

An amorphous phase precedes crystallization; unraveling the colloidal synthesis of zirconium oxide nanocrystals

Rohan Pokratath,[†] Lermusiaux Laurent,[‡] Jikson Pulparayil Mathew,[†] Stefano Checchia,[¶] Susan Rudd Cooper,[§] Jette Katja Mathiesen,[§] Guillaume Landaburu,[‖] Soham Banarjee,[⊥] Songsheng Tao,[#] Nico Reichholf,[†] Simon J. L. Billinge,[#,@] Benjamin Abécassis,[‡] Kirsten M. Ø. Jensen,[§] and Jonathan De Roo[*,†]

†*Department of Chemistry, University of Basel, Mattenstrasse 24a, 4058 Basel, Switzerland*

‡*Laboratoire de Chimie, ENS de Lyon, CNRS, 46 allée d'Italie, 69364 Lyon, France*

¶*ESRF Synchrotron, ID15A Beamline, Avenue des Martyrs, CS40220, 38043 Grenoble, France*

§*Department of Chemistry, University of Copenhagen, Universitetsparken 5, 2100 Copenhagen Ø, Denmark*

‖*Univ Lyon, ENS de Lyon, CNRS, Université Claude Bernard Lyon1, Laboratoire de Chimie, Lyon, France*

⊥*Deutsches Elektronen-Synchrotron DESY, Notkestraße 85, 22607 Hamburg, Germany*

#*Applied Physics and Applied Mathematics Department, Columbia University, New York, NY, USA*

@*Condensed Matter Physics and Material Science Department, Brookhaven National Laboratory, Upton, NY, USA*

E-mail: Jonathan.DeRoo@unibas.ch

Abstract

One can nowadays readily generate monodisperse colloidal nanocrystals, but the underlying mechanism of nucleation and growth is still a matter of intense debate. Here, we combine X-ray pair distribution function (PDF) analysis, small angle X-ray scattering (SAXS), nuclear magnetic resonance (NMR), and transmission electron microscopy (TEM) to investigate the nucleation and growth of zirconia nanocrystals from zirconium halide and zirconium isopropoxide at 340 °C, in the presence of surfactant. We find that many *amorphous* particles are initially formed. Over time, the particle concentration decreases. The amorphous particles recrystallize into nanocrystals and the concentration of nanocrystals stays constant over the course of the reaction. Both findings stand in contrast to reports of continuous nucleation in other surfactant-assisted nanocrystal syntheses. The non-classical nucleation is likely related to the precursor decomposition rate that is an order of magnitude higher than the crystallization rate. Comparing different halide sources, we observe higher rate constants for zirconium bromide compared to zirconium chloride, resulting in smaller particles with lower polydispersity.

Introduction

A surfactant-assisted synthesis of nanocrystals is a complex sequence of reactions that usually starts with the conversion of molecular precursors. It is often hypothesized that the precursor conversion results in a single unit of the final material; the *monomer*. According to classical nucleation theory, the monomer is in thermodynamic equilibrium with the formed particles. First, the monomer builds up in solution, above the equilibrium solubility, until reaching a critical supersaturation. Lamer hypothesized that at this point, particles homogeneously nucleate (infinitely fast) and after this *burst nucleation*, the particles grow via diffusion-limited growth.[1] The intrinsic limitations of the Lamer model and classical nucleation theory have been reviewed at length.[2,3] Convincing disproof for burst nucleation has been recently

provided by Small Angle X-ray scattering (SAXS) and UV-Vis spectroscopy, showing a continuous increase in the number of Pd, InP, CdSe, and PbS(e) nanocrystals over a large portion of the reaction time.[4–9] Continuous nucleation, when coupled with a strongly size-dependent growth rate, is not necessarily at odds with classical nucleation theory (*i.e.*, thermodynamic equilibrium).[5] It is inconsistent with the burst nucleation hypothesis.

Kinetic models with irreversible reactions have also been developed to describe nucleation. The Finke-Watzky two-step model features slow, continuous nucleation and fast, autocatalytic growth.[10] This model, where growth involves the direct reaction of the precursor (not a momomer) with the nanocrystal surface, could describe the sigmoidal kinetics of metal nanocrystal formation.[4,10] By including size-dependent growth rates and ligand binding equilibria, the particle size (distribution) could be modeled.[4,11]

The nonclassical nucleation of calcium phosphate from Ca^{2+} and phosphate (in water) involves pre-nucleation clusters, which assemble in polymeric structures. Amorphous particles nucleate and subsequently recrystallize.[12] The synthesis of magnetite nanocrystals features the aggregation of 2 nm primary particles directly in crystalline particles.[13] An order-disorder equilibrium (between an amorphous and crystalline state) was observed by in situ TEM during the nucleation of Au nanocrystals, indicating that crystallization is not irreversible.[14] Note that these studies were performed in the absence of ligands. Using liquid cell TEM, an amorphous phase was also detected in the synthesis of Ni nanocrystals with oleylamine ligands.[15]

Some thermodynamic models consider the final nanocrystal size as an equilibrium product, the size of which is determined by the amount and type of surfactant. The thiol-to-gold ratio for example determined the final size of Au nanocrystals.[16] Self-focusing via ripening was also observed in the synthesis of MnO nanocrystals, where the number of particles decreases over the course of the reaction.[17] Also in the heat-up synthesis of CdSe nanocrystals from cadmium myristate and selenium, a decreasing particle concentration was observed after an initial, steep increase. 72 % of initially formed particles were consumed in this process,

while the size distribution narrowed.[18] These models present the monomer as a shuttle for particle growth. The monomer is assumed to be formed by the dissolution of particles and can reattach to a different particle.

Oriented attachment and coalescence are two growth mechanisms that do not involve growth by monomer.[19,20] For example, oriented attachment was observed for ZnO and TiO_2,[21–23] in the absence of ligands, or for ZnS in oleylamine, a ligand that is typically weakly bound.[24] Coalescence was shown for Ir and Pt nanocrystals, again with weakly binding ligands.[25,26] Especially in the case of Pt, a detailed TEM analysis showed an initial increase in the number of particles and a subsequent decrease, mostly caused by coalescence and to a minor extent by particle dissolution.[26] Some particles grew by monomer/precursor attachment and others by coalescence. While regular growth immediately forms single crystalline particles, a polycrystalline particle is initially observed after coalescence. Structural rearrangement took about 16 seconds after coalescence to produce a single crystalline nanocrystal. Irrespective of the mechanism, the nanocrystals stopped growing after reaching a certain size (*i.e.*, self-focusing).

In the synthesis of iron oxide nanocrystals from iron oleate, the precursor is an iron oxo cluster with three iron atoms connected by a μ_3-oxygen atom.[27] Esterification of the oleate leads to a continuous growth of the precursor into nanocrystals, without a separate nucleation step. Continuous growth was also observed in indium oxide nanocrystal synthesis where indium oleate is slowly added to hot alcohol.[28] After the initial formation of In_2O_3 particles, the number of particles remains constant whereas the precursor is continuously added and the nanocrystal grow in a highly controlled way. Dopants can be precisely positioned in the nanocrystal. In this case, the reaction is probably not limited by diffusion or reaction rates but rather by the precursor addition rate.

The formation mechanism of (yttria stabilized) zirconia nanopowders has previously been studied using *in situ* X-ray total scattering with Pair Distribution Function (PDF) analysis.[29,30] Using a surfactant-free, solvothermal method, ZrO_2 was synthesized from zirconium

oxynitrate in methanol. The polymeric precursor complex converts into amorphous particles with a local structure similar to that of monoclinic zirconia.[29,30] After crystallization, particles with the cubic crystal structure were retrieved. A similar reaction route was found in a hydrothermal synthesis from zirconia acetate, although the kinetics of the reactions were different. Furthermore, polymorphism in pure zirconium oxide was linked to whether the local order of the disordered intermediate persisted or changed during crystallization.[29]

Little is known about the surfactant-assisted synthesis of group 4 metal oxides. For example, highly monodisperse and colloidally stable zirconia nanocrystals are synthesized from zirconium chloride and zirconium isopropoxide (complexed with isopropanol) at 340 °Cin trioctylphosphine oxide (TOPO).[31] We recently showed that a mixed chloroalkoxide precursor species is formed, which undergoes (predominantly) E1 elimination to zirconium hydroxide and propene, see Scheme 1.[32] After ligand redistribution and condensation, zirconium chloride, zirconium oxide, and isopropanol are formed as products. The $ZrCl_4$ co-product is retrieved as a complex of TOPO,[32] and also the nanocrystals are covered with TOPO and some of its decomposition products.[33] There is no information about their nucleation and growth mechanism. Understanding these processes might help to further control the nanocrystal size, introduce dopants and access the core-shell structures of group 4 oxides. Since also titania and hafnia nanocrystals can be synthesized by similar routes, the zirconia model system is relevant for the entire group 4. Within this context of group 4 oxides, a Lewis structure of a MO_2 "monomer" is hard to conceive. A slightly more realistic monomer could be, e.g., $Zr(OH)_4$, but group 4 metal hydroxide species are highly reactive and usually already condense before the tetrahydroxide species can be fully formed.

Here, we investigate the crystallization mechanism of zirconia nanocrystals in TOPO, synthesized from zirconium halide (chloride or bromide) and zirconium isopropoxide. We combine X-ray pair distribution function analysis, small angle X-ray scattering, nuclear magnetic resonance, and transmission electron microscopy to investigate their nucleation and growth. In order to assign the crystallization mechanism to one of the earlier prposed

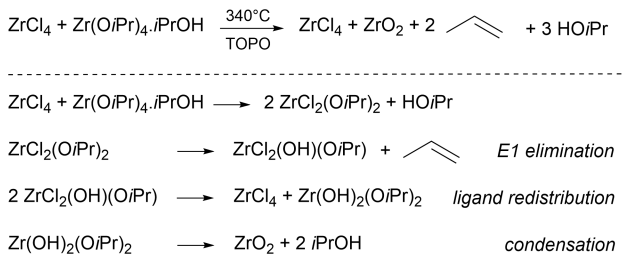

Scheme 1: The synthesis of zirconia from zirconium chloride and zirconium isopropoxide isopropanol complex at 340 °Cin tri-octylphosphine oxid (TOPO). The chemical mechanism involves first the formation of mixed chloro-alkoxide species, which undergo E1 elimination, ligand redistribution, and condensation reactions.[32]

mechanisms, we determined the temporal evolution of the number of particles, the particle size and the yield. We find that after an initial fast increase in the number of particles, the particle number drops again with a concomitant reduction of the size dispersion. While the first particles are amorphous, the final particles are monocrystalline.

Results and Discussion

Following Scheme 1, we synthesize zirconia nanocrystals at 340°C, from a 1:1 molar mixture of $Zr(OiPr)_4 \cdot iPrOH$ with either (i) $ZrCl_4$ or (ii) $ZrBr_4$.

Small angle X-ray scattering

Given the success of small angle X-ray scattering (SAXS) in delivering insights into nucleation and growth mechanisms,[4,5,8,9] we also take it here as a starting point. We performed *ex situ* SAXS measurements on aliquots, taken from the reaction mixture at 300°C, 320°C, and 340°C during the heating ramp, and at different time intervals at 340 °C. The samples were measured in a flow-through setup to obtain signals in absolute intensity (Fig. 1A-B) and to estimate the particle concentration and size (see experimental section and SI for details).[34]

Qualitatively, the evolution of the scattering curves with time suggests the formation of spherical particles. Over the course of the reaction, the signal resembles more and more the

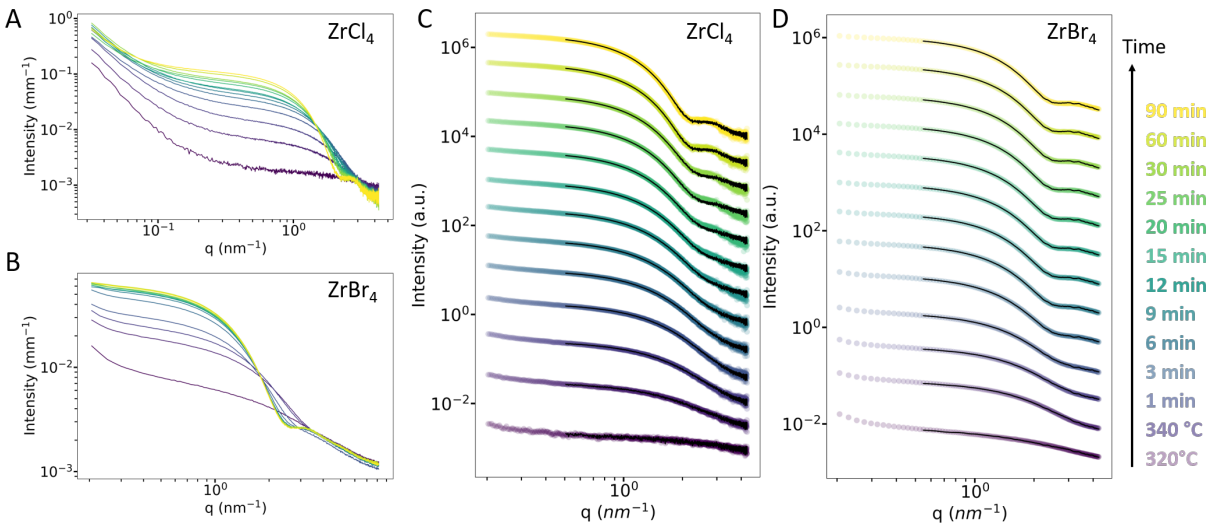

Figure 1: Normalized SAXS measurements of reaction aliquots (A-B) and corresponding fits (C-D) for reaction mixtures with either $ZrCl_4$ or $ZrBr_4$. The different patterns are shifted with respect to one another for a better visualization.

form factor of a sphere with a plateau at intermediate q and an abrupt decrease followed by oscillations for q larger than 2 nm^{-1}. Both the increase of the plateau intensity with time and the shift of the position of the abrupt decrease toward smaller q indicate particles growing in size. The amplitude increase of the oscillations suggests that the polydispersity decreases with time.

The particle size and concentration were quantified by fitting the normalized scattering curves. At lower q, we observe an increase in the intensity (Figure 1A-B), which probably results from a partial aggregation of the particles. This would require introducing a structure factor in the fit. To minimize this effect and to consider a model of independent scatterers, our experimental data is fitted in the q region larger than 0.5 nm^{-1}. The SAXS patterns contain contributions from precursors and zirconia particles in solution:

$$I \approx I_{particles} + I_{precursors}$$

To approximate the signal of the precursors, we use the experimental SAXS signal of the $ZrCl_4$ reaction mixture, aliquoted at 300 °C. At this temperature, precursor conversionn

has not yet started.[32] Therefore, our fitting function becomes the sum of the scattering cross section of a distribution of polydisperse spheres and the experimental precursor signal, multiplied by a fitting parameters (F) set between 0 and 1:

$$I_{fit} = I^{theor}_{spheres} + F \times I^{exp}_{precursors}$$

This approach leads to very good fits for all the SAXS patterns (Fig. 1C-D), allowing us to derive the particle radius, concentration and polydispersity during the synthesis, for both systems (Figure 2).

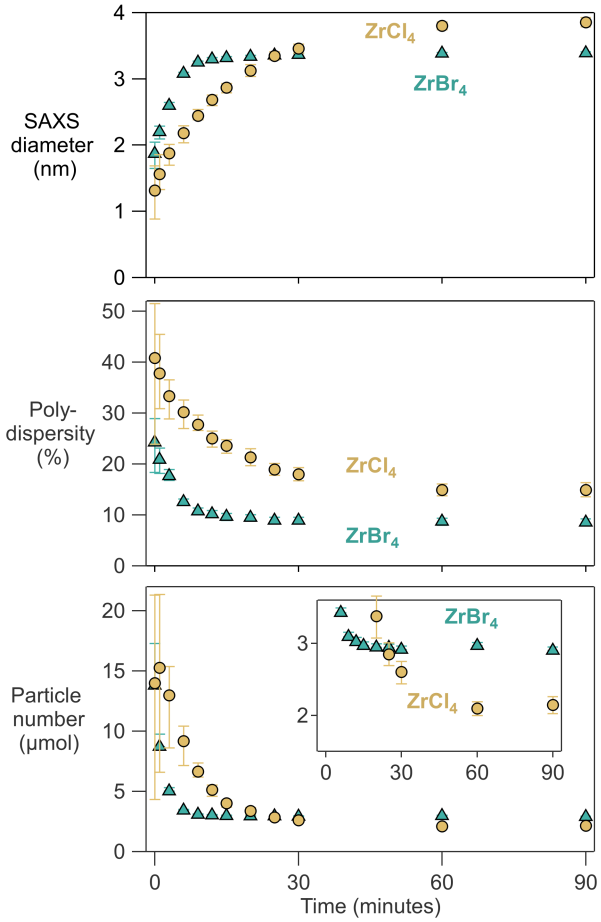

Figure 2: Time evolution at 340°C of the particle size, the particle concentration, and the polydispersity obtained by SAXS measurements for the synthesis with either $ZrCl_4$ or $ZrBr_4$ as halide source.

For both reactions (with either $ZrCl_4$ or $ZrBr_4$ as halide source), there are particles

present in the solution once the reaction temperature reaches 340 °C. We observe particle growth (increase in diameter) with a simultaneous reduction in the polydispersity (Figure 2). The higher polydispersity in the first 10 minutes is also responsible for the higher error on the diameter value. The final particle size obtained in the $ZrCl_4$ (3.9 nm) reaction is higher than the $ZrBr_4$ (3.4 nm) reaction, consistent with previous reports.[31] The particles in the chloride reaction mixture keep growing for 90 min, while the growth of the bromide particles stops after about 15 min. Interestingly, the particle number *decreases* over the course of the reaction. These results stand in stark contrast to many other surfactant-assisted nanocrystal syntheses, which featured a continuous *increase* of the particle concentration (evidence for continuous nucleation).[4–8] Our data thus rather suggests a coalescence or ripening mechanisms.[17,18,26] A lot of particles have nucleated at the start and grow at the expense of other particles. When comparing the two halide sources, the particles from the bromide reaction grow faster, have a lower dispersity, are smaller in size and their final concentration is higher. For the same material yield, one can have either few, large particles or many, small particles. The particle concentration at the end of the bromide reaction is indeed about 50 % higher than in the chloride reaction (Fig. 2), consistent with their diameter difference.

X-ray pair distribution function analysis

X-ray total scattering and pair distribution function (PDF) analysis are great tools for understanding the chemistry of nucleation.[35] In our previous work, we used PDF analysis to confirm the chloroalkoxide precursor and the $ZrCl_4 \cdot 2\,TOPO$ byproduct.[32] At room temperature, the PDF of the chloride reaction mixture features three inter-atomic distances; Zr-O (2.0 Å), Zr-Cl (2.5 Å) and Zr-P (3.5 Å), as expected for the $ZrCl_2(O\mathit{i}Pr)_2 \cdot 2\,TOPO$ precursor species. These atom pairs can still be recognized in the PDF of the first aliquot taken at 340 °C, see Figure 3 (0 min). We observe similar atomic pair distances for the reaction mixture with $ZrBr_4$ but the Zr-Br distance is a bit longer: 2.7 Å (Figure 3, 0 min).

After reaching 340 °C, there are not yet crystalline particles present. However, within

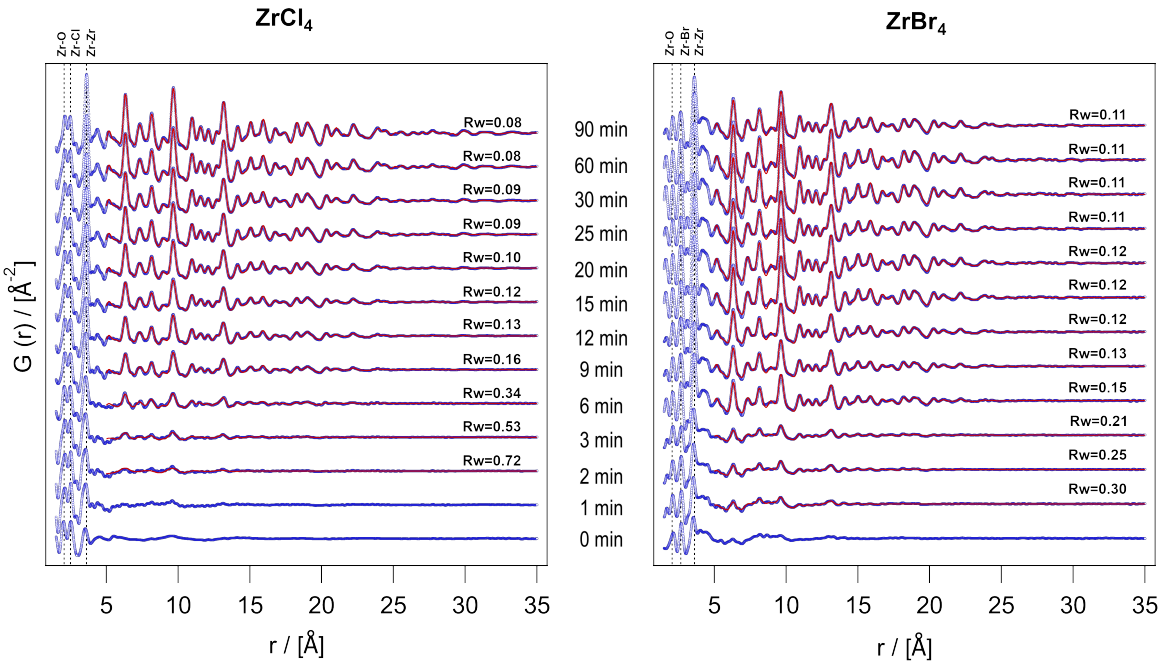

Figure 3: PDFs of reaction aliquots from the reaction with either $ZrCl_4$ or $ZrBr_4$. The experimental PDF is represented by the blue circles, and the fitted PDF by the red line. The goodness of fit is indicated by Rw. The reaction temperature of 340 °C is reached at t = 0 min. The refined parameters are shown in Table S1-S2.

minutes, zirconia crystals start to form and grow in size, indicated by the appearance of correlations at higher distances (Figure 3). The Zr-Cl and Zr-Br distances contract slightly but remain present until the end of the reaction and are assigned to the TOPO complexes of $ZrCl_4$ and $ZrBr_4$. For the chloride reaction this complex is $ZrCl_4 \cdot 2\,TOPO$. For the bromide reaction, the exact nature of the complex is unclear since the complexation between $ZrBr_4$ and TOPO is not fully understood (**Figure S3**). Nevertheless, the ^{31}P NMR spectrum at the end of the reaction, is almost identical to the spectrum of $ZrBr_4$ and 8 TOPO equivalents. Therefore, we conclude that the metal halide is formed as the by-product, in both cases. we infer that the reaction with $ZrBr_4$ likely follows a similar precursor conversion mechanism as the reaction with $ZrCl_4$ (Scheme 1). Previously, we have shown that the PDF of the last aliquots (end of reaction) can be well described by a two-phase model, featuring (i) tetragonal ($P4_2/nmc$) zirconia and (ii) the $ZrCl_4 \cdot 2\,TOPO$ complex.[32] This approach does not work as well for the bromide case, since we do not have an accurate structure for the

TOPO complex of $ZrBr_4$.

To quantify the crystal size, all aliquot PDFs are refined (see the red lines in Figure 3). The two-phase modeling strategy appears to be less successful for the early aliquots, even in the chloride reaction. The contribution of the crystal phase is low and the molecular zirconium precursors species are not yet fully converted in the $ZrCl_4 \cdot 2\,TOPO$ by-product. For this reason, we start the fit from 5 Å, cutting off the contributions from the molecular precursors and only focusing on the tetragonal zirconia phase, see Figure 3. For the bromide case, we follow the same strategy but we add a decaying sinusoid to the model. The latter takes care of a periodic oscillation in the data. Similar effects were previously reported and attributed to solvent restructuring induced by colloidal nanoparticles.[36] It is unclear why this effect is stronger for the bromide case. The refined particle size and goodness of fit (Rw) are shown in Figure 4. In the chloride reaction mixture, we could not obtain a decent refinement for the aliquots taken at 0 and 1 min. Only after 2 min, we can discern the first features of a nanocrystal of about 1.8 nm in diameter. The crystal pattern is fairly weak (due to a low concentration of crystals), which is reflected in the poor (high) Rw of the refinement. The particles grow over time to the expected crystal diameter of about 4 nm, and the Rw of the refinements decreases to 8%. The PDF of the bromide reaction mixture could not be refined at t = 0 min. After 1 min, we are able to refine the PDF reasonably well (Rw = 0.3) and the first observable nanocrystal is also 1.9 nm in diameter. We are careful not to interpret these crystals as "the nuclei". It is simply the size of the first observable coherent scattering domain. Although PDF is perfectly suited for short-range structures and could thus pick up smaller crystals, it is possible that such smaller structures are present at too low concentrations. The bromide reaction forms crystalline material faster than the chloride reaction, but the particles are growing only to about 3.3 nm in size. The bromide nanocrystals reach their final size after about 30 min, while the chloride particles keep growing for up to 90 min. This is even more obvious when the nanocrystal volume is plotted over time (**Figure S4**). The obtained crystal size from PDF at various time points is

in agreement with the size calculated from the TEM images of purified nanocrystals (**Figure S5**).

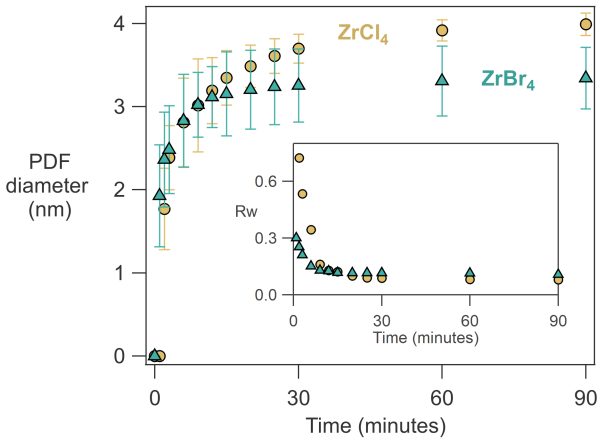

Figure 4: Refined nanocrystal size by PDF and corresponding Rw values (inset) for reaction mixtures with either $ZrCl_4$ or $ZrBr_4$. The data points that could not be refined are represented by a diameter of 0 nm.

We also followed the reaction *in situ* in a 3 mm NMR tube heated by an aluminum metal block with heating cartridges (see experimental and **Figure S6**). Similar trends are observed (see **Figure S7**) but in general, the signal-to-noise ratio is much lower compared to the *ex situ* experiments. Most importantly, we conclude that no phase transformation took place in the crystals upon quenching the reaction aliquots to room temperature.

The emergence of an amorphous phase

Comparing the results from SAXS and PDF, we are forced to conclude that they do not agree (at first sight). Upon reaching 340 °C (t = 0 min), SAXS reveals the presence of nanoparticles, while PDF demonstrates the absence of nanocrystals (no long range correlations). SAXS detects any nanoparticles, crystalline or amorphous. We thus hypothesize that the first particles observed by SAXS are amorphous (*i.e.*, disordered). To investigate this hypothesis further, we turn now to the short-range PDF data (1.5 – 5 Å). This complex region contains contributions from precursors, by-products, crystalline (ordered) particles,

and amorphous (disordered) particles. To reduce the complexity, we first analyze the chloride reaction aliquot at t = 9 min (Figure 5). We know that after 9 min there is no precursor left and the only molecular zirconium species is the by-product $ZrCl_4 \cdot 2\,TOPO$ (**Figure S8**).[32] The absence of precursors simplifies the PDF analysis. To extract the contribution of the amorphous particles, we proceed as follows.

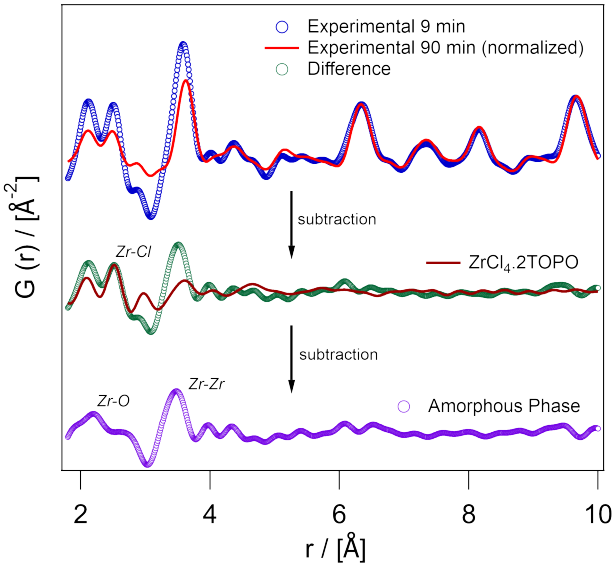

Figure 5: The short-range PDF of the 9 min aliquot (chloride reaction). The blue circles represent the measured PDF of the aliquot, the red line corresponds to the PDF of the reaction crude product (90 min aliquot). After subtraction of the two, the data in green is obtained. The PDF of the $ZrCl_4 \cdot 2\,TOPO$ by-product (brown line) is scaled and subtracted from the green data, yielding the PDF of the amorphous intermediate (violet circles).

We scale the PDF of the final aliquot (90 min) to match the intensity of the peaks beyond 5 Å(Figure 5. A significant deviation is observed in the short r-range (1.5 - 5 Å). We then subtract the two PDFs and obtain the green data. This procedure completely removes the crystalline fraction and part of the $ZrCl_4 \cdot 2\,TOPO$ by-product. The latter is only partially removed due to the difference in relative concentration of crystals and by-product at the two time points. Therefore, we scale the experimental PDF of $ZrCl_4 \cdot 2\,TOPO$ to the Zr-Cl peak in the green data and subsequently subtract it. We thus arrive at the residual PDF, free of crystals and by-product. Since also precursor is absent (evidenced by NMR), the residual PDF belongs to the amorphous intermediate. We exclude the possibility of a monomer

due to the pronounced Zr-Zr distance in the PDF. No long-range order is present in the PDF of the amorphous phase. At this point, we hypothesize that the amorphous particles are intermediates *en route* to the crystalline particles. We extended the analysis to other aliquots, see **Figure S9**. With time, the crystalline phase captures a higher proportion of the short-range structure, confirming that the amorphous phase is an intermediate that disappears. To rule out the possibility of amorphization while sampling/cooling down, similar analyses were carried out on the *in situ* data set and similar results are obtained **Figure S11**.

Precursor decomposition

It is often assumed that the precursor-to-monomer (P to M) conversion kinetics are slower than the crystallization kinetics.[37,38] This is an accepted prerequisite for controlling the size by the reaction rate.

$$\mathrm{P} \xrightarrow{slow} \mathrm{M} \overset{fast}{\rightleftharpoons} \mathrm{NC} \tag{1}$$

To quantity the precursor conversion kinetics in our system, we followed the disappearance of the isopropoxide resonance in ^{1}H NMR, see Figure 6 (Corresponding ^{1}H spectra are shown in **Figure S12-13**). We observe faster kinetics with $ZrBr_4$, compared to $ZrCl_4$. Even during the heating phase to 340 °C, the bromide reaction mixture starts to convert at 200 °C, while the chloride reaction only starts converting between 300 and 340 °C. Consequently, at t = 0 min, the bromide reaction progress is already about 80 %. Interestingly, the bromide reaction slows down considerably by the end of the precursor conversion. For both precursors, full conversion is achieved after 9 min at 340 °C.

The mass balance of the reaction

Earlier we postulated that the amorphous particles are intermediates in the reaction. To confirm this hypothesis, we sought to quantify all zirconium species in the reaction and have

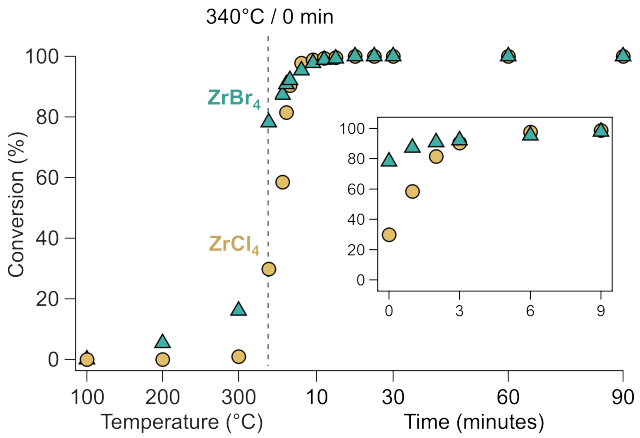

Figure 6: The precursor conversion (disappearance of zirconium isopropoxide) as determined by NMR. The inset aims at showing more detail for the first 9 minutes of reaction time at 340 °C.

a closed mass balance. In Figure 7, we plot the precursor conversion by NMR and the yield determined by SAXS and total scattering. We calculated the total particle yield from the SAXS data using the particle size, the size distribution and the particle concentration assuming the bulk density of zirconia. For the end of the reaction, we obtain a yield (n_{ZrO_2}/n_{Zr}) of 63% with $ZrCl_4$ and 58% with $ZrBr_4$, consistent with the obtained yield after isolation and purification (determined gravimetrically). We know the zirconium halide by-product is responsible for the lower than 100% yield (based on metal). Therefore, the unbiased results from SAXS satisfy the mass balance of zirconium according to Scheme 1. To focus on the oxide formation, we re-scaled the yield from SAXS to 100% at the end of the reaction, which also corresponds to 100% precursor conversion. The rate of precursor conversion is equal to the rate of particle formation since the precursor conversion data and the total particle (SAXS) data coincide, within error. This means that, at any time, all the zirconium atoms are either in the form of precursor or part of a particle (amorphous or crystalline). We do not find evidence for another species such as molecular solute or a "monomer".

We calculated the yield of crystalline particles from the total scattering data, by integrating the area under a selected Bragg peak (**Figure S14)** after background subtraction. Also here, we scale the yield to 100% at the end of the reaction. This assumes that no amorphous

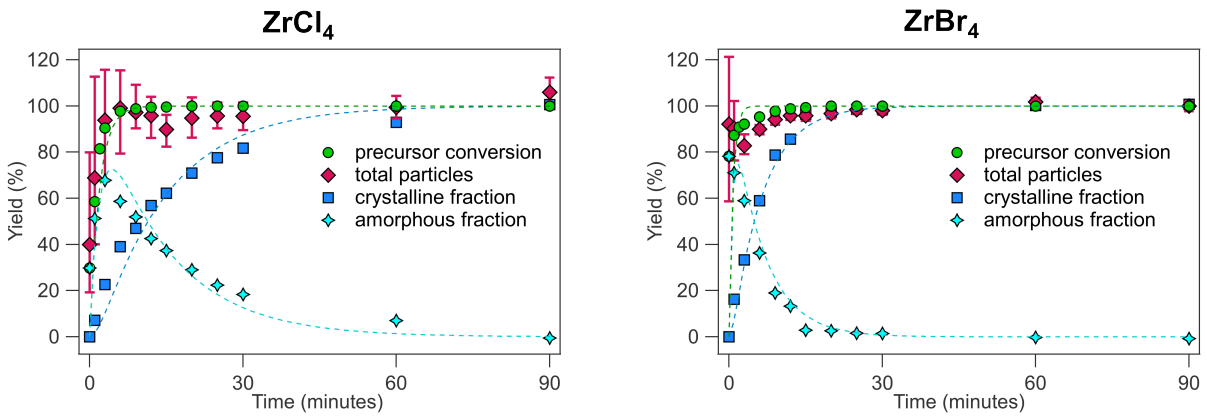

Figure 7: The yield of the reaction, from the perspective of precursor conversion, the total particles formed (from SAXS data), the crystalline fraction (from total scattering data), and the amorphous fraction (total particles minus crystalline fraction).

phase is present at the end of the reaction. It is a fair approximation given that the PDF of the last reaction aliquot could be accurately modeled by only the crystalline phase and the zirconium chloride by-product.[32] We then calculate the amorphous fraction of particles by subtracting the crystalline fraction from the total particle yield. Given our conclusion that precursor conversion and total particle yield are identical, we used here the precursor conversion yield for the subtraction, since there is less scatter on this data.

For the chloride reaction, the precursor conversion is complete at 9 min, but the crystalline yield is only about 50%. In addition, there is no evidence for a monomer. Hence this reaction is not well described by Equation 1. Instead, precursor conversion is clearly faster than crystallization. Since the species formed by precursor conversion (metal hydroxide) is highly reactive, this leads to a build-up of amorphous intermediate (I). The intermediate then slowly recrystallizes into nanocrystals, see Equation 2.

$$\mathrm{P} \xrightarrow[k_1]{fast} \mathrm{I} \xrightarrow[k_2]{slow} \mathrm{NC} \tag{2}$$

Similar conclusions are reached for the bromide reaction although the crystallization rate appears faster.

To obtain more quantitative insight in the reaction kinetics, we modeled the time-

dependent concentration of species. Starting from the simplest model containing two elementary steps (Mechanism 3), we can reasonably well describe the kinetics of both the chloride and the bromide reaction.

$$\begin{aligned} \mathrm{P} &\xrightarrow{k_1} \mathrm{I} \\ \mathrm{I} &\xrightarrow{k_2} \mathrm{NC} \end{aligned} \tag{3}$$

The resulting fit is plotted onto Figure 7 as dotted lines (and also plotted in **Figure S15 and S21**). The rate constants are provided in Table 1. The bromide crystallization rate constant (k_2) is about double compared to the chloride crystallization rate constant. In both cases, the precursor conversion rate constant is one order of magnitude higher than the crystallization rate constant, which is in disagreement with the classical dogma in Equation 1.

Table 1: Comparison of reaction rates for zirconium oxide nanocrystal formation from $ZrCl_4$ and $ZrBr_4$ as the precursors. The unit of the first order rate constants is min^{-1}. The unit of the second order rate constants is mM^{-1} min^{-1}

Mechanism	**Precursor**	k_1	k_2	k_3
(3)	$ZrCl_4$	0.53 ± 0.013	0.074 ± 0.002	-
(3)	$ZrBr_4$	1.380 ± 0.051	0.167 ± 0.015	-
(4)	$ZrCl_4$	0.529 ± 0.010	0.281 ± 0.011	0.061 ± 0.018
(5)	$ZrBr_4$	7.4 ± 0.138	0.281 ± 0.024	1.046 ± 0.085

Focusing on the chloride reaction, we tested multiple other mechanisms to explore the possibility of second order reactions, equilibria and auto-catalytic mechanisms (Figures S16-S20). Taking the precursor conversion as second order, we obtain a considerably worse fit (**Figure S16**). This give us further confidence in the E1 elimination mechanism since the latter should be first order. A mechanism that includes an equilibrium between precursors and intermediates does not fit significantly better than Mechanism 3 (**Figures S18**). The back reaction (I $\longrightarrow$ P) has an almost negligible rate constant. The fit improved when taking the crystallization step as second order (**Figure S17**). Finally, the best agreement

was obtained with Mechanism 4 (**Figure S20**).

$$\begin{aligned} \mathrm{P} &\xrightarrow{k_1} \mathrm{I} \\ 2\,\mathrm{I} &\xrightarrow{k_2} 2\,\mathrm{NC} \\ \mathrm{I} + \mathrm{NC} &\xrightarrow{k_3} 2\,\mathrm{NC} \end{aligned} \tag{4}$$

The precursor conversion is first order, the second step is second order (a coalescence nucleation mechanism) and the third step is autocatalytic growth by addition of the amorphous species. The rate constants are reported in Table 1. Although Mechanism 4 has some resemblance to the Finke-Watsky (FW) mechanism,[10] there is an important difference. The FW mechanism typically features a slow nucleation step that can be six orders of magnitude slower than the autocatalytic growth. Here, we find that k_2 is five times higher than k_3.

We also explored different mechanisms for the bromide reaction (**Figures S21-S26**). The precursor conversion reaction is not well described by first order kinetics. The data is better described by a second order process (**Figure S22**), or by an equilibrium between precursor and intermediate (**Figure S24**). We cannot distinguish between the two scenarios based on the current data. Taking the precursor conversion as second order, we considered the crystallization to be second order (**Figure S23**) or autocatalytic (**Figure S25-S26**) and the best fit was found for Mechanism 5.

$$\begin{aligned} 2\,\mathrm{P} &\xrightarrow{k_1} 2\,\mathrm{I} \\ 2\,\mathrm{I} &\xrightarrow{k_2} 2\,\mathrm{NC} \\ \mathrm{I} + \mathrm{NC} &\xrightarrow{k_3} 2\,\mathrm{NC} \end{aligned} \tag{5}$$

Interestingly, k_2 is refined to the same value as for the chloride reaction but k_3 is much higher for the bromide reaction.

Nucleation and growth mechanism

The first observable crystal size from PDF is 1.8 nm. Before observing crystals, SAXS already detected large amounts of amorphous particles present in the reaction mixture. This intermediate material is a logical consequence of the high reactivity of Zr-OH moieties. The size of the amorphous particles was determined to be 1.5 - 2 nm, close to the first observable crystal size. It is not unreasonable to assume that an amorphous particle crystallizes while maintaining its size. However, it is clear that the number of particles decreases over the course of the reaction, see Figure 2. This must happen via either a coalescence or a dissolution process. Distinguishing the two mechanisms is not straightforward with the data at hand. In the case of zirconium chloride, our kinetics modeling does suggest that a reversible equilibrium between intermediates and precursors is less likely than intermediates reacting with themselves or growing onto nanocrystals, thus rather supporting a coalescence mechanism.

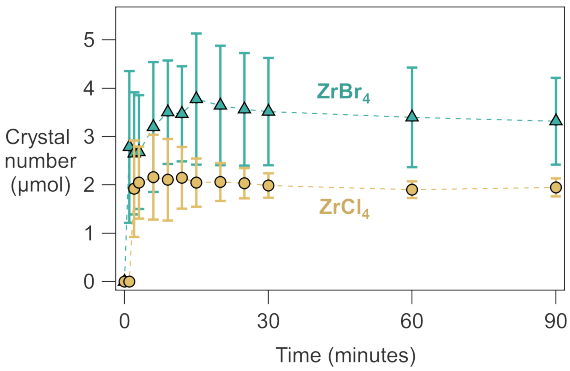

Figure 8: The number of nanocrystals as a function of time, calculated from the crystalline yield and the crystal size (PDF).

It is interesting to see that the number of crystalline particles (Figure 8, calculated from the crystalline yield and the crystal size) stays constant for the chloride reaction. There is more scatter on the crystal number in the bromide case, but there the error on the size is larger due to the more complex PDF refinement. It might be reasonable to say it also remains fairly constant. Therefore, we conclude that the number of particles in these reactions is

set by a nucleation event, which happens soon after reaching 340 °C. The nucleation is faster than the time resolution in our data (Figure 8) and we do not have information on its kinetics. Given that the number of nanocrystals does not change, the final nanocrystal size is set by this nucleation event. A larger number of nanocrystals correlates with a smaller final size.

Overall, we see no evidence for continuous nucleation nor for coalescence or ripening of the *crystalline* particles. We conclude that the decrease in the total particle number (determined from SAXS, Figure 2) is due to the disappearance of amorphous particles, causing growth of the nanocrystals. A schematic representation of the proposed mechanism is given in Figure 9.

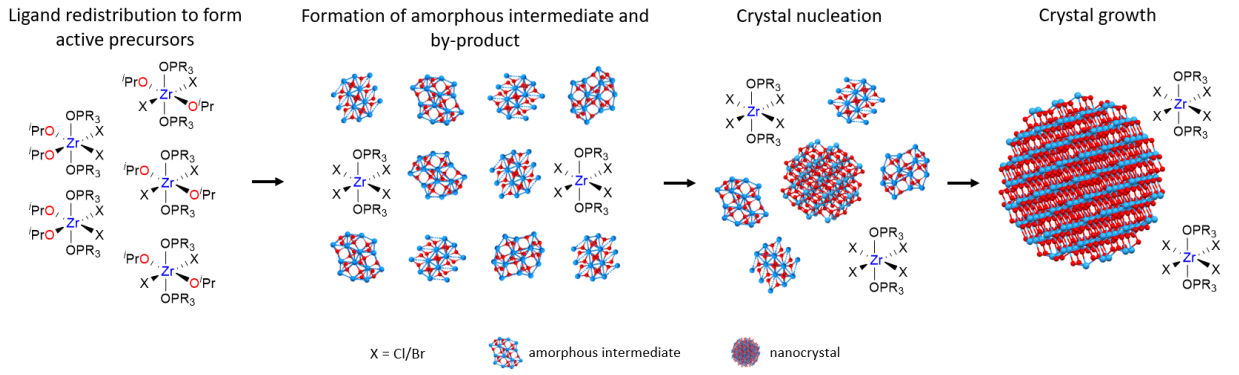

Figure 9: Schematic representation of the formation mechanism of zirconia nanocrystals.

Conclusion

We elucidated the nucleation and growth mechanism during the non-aqueous synthesis of ZrO_2 nanocrystals from zirconium halide (chloride and bromide) and zirconium isopropoxide in trioctylphosphine oxide. Upon decomposition of the active precursor, a lot of amorphous nanoparticles are formed, which are subsequently converted into nanocrystals. The presence of the amorphous intermediate was evidenced by a combined analysis of X-ray total scattering, small-angle X-ray scattering, and NMR. We determined that the precursor conversion

rate is an order of magnitude higher than the crystallization rate. This rate imbalance is responsible for the rapid build-up of amorphous particles. Changing the halide precursor from chloride to bromide, we observed faster kinetics of both precursor conversion and crystallization, together with a smaller crystal size. We found that the size difference is due to a difference in nucleation events. The bromide reaction nucleates more nanocrystals than the chloride reaction and the number of nanocrystals does not significantly change during the reaction.

Experimental

Materials. $ZrCl_4$(99.9 %) and $ZrBr_4$(99 %) were purchased from Strem Chemicals and $Zr(OiPr)_4$.iPrOH (99.9 %), toluene (99.5 %), acetone (99.8 %) from Sigma Aldrich and used without further purification. Deuteroform (99.8 atom %) was purchased from Cambridge Isotope laboratories and Benzene-D6 (99.5 atom %) from Apollo scientific, 10/100 mL of activated 4 Å molecular sieves were added and left to stand for 3 days in the glovebox to remove residual water. 3 mm high-throughput NMR tubes (0.58 mm wall thickness) were purchased from Sigma Aldrich. Tri-n-octylphosphine oxide (99 %) was bought from Strem chemicals and recrystallized according to Owen et. al.[39] $ZrCl_4$.2THF was synthesized according to Manzer et al.[40]

Instrumentation. Transmission electron microscopy (TEM) imaging was done using a JEOL JEM2800 field emission gun microscope operated at 200 kV equipped with a TVIPS XF416ES TEM camera. Nuclear Magnetic Resonance (NMR) measurements were recorded on Bruker spectrometers operating at a 1H frequency of 500.13 MHz. 31P spectra were acquired using inverse gated decoupling. The 31P spectra were processed with a line broadening of 5 Hz to reduce noise.

ZrO_2 synthesis. Zirconia nanocrystals are synthesized according to previously published procedures.[31,33] Typical amounts were 10 g recrystallized TOPO, $Zr(OiPr)_4$.iPrOH

(0.775 g, 2 mmol), and $ZrCl_4$.2THF (0.943 g, 2.5 mmol). Synthetic variations include (i) using only $ZrCl_4$.2THF (0.754 g, 2 mmol), (ii) using $ZrCl_4$ (0.466 g, 2 mmol) instead of $ZrCl_4$.2THF, and (iii) using $ZrBr_4$ (0.821 g, 2 mmol) instead of $ZrCl_4$.2THF.

***Ex situ* X-ray total scattering experiments.** Samples were prepared by the temporal sampling of reaction aliquot into 3mm NMR tubes and sealed under Argon atmosphere. We also used 2 mm glass capillaries from Hilgenberg for sampling, but they were prone to breaking and the data quality was not worse. The samples were measured either using beamline P21.1 at DESY in Hamburg, Germany, or using beamline ID15 at ESRF in Grenoble, France. At ESRF, ex-situ X-ray scattering data were collected at 80 °C (using a nitrogen cryo stream), in rapid acquisition mode, using a 2D Pilatus CdTe 2M detector (172 × 172 μm pixel size) with a sample-to-detector distance of 264 mm. The incident wavelength of the X-rays was $\lambda = 0.1441$ Å (66.05 keV). Calibration of the experimental setup was performed using a Silicon standard sample. At DESY, ex-situ X-ray scattering data were collected at 80 °C in a home-built aluminium heating block (see in situ experiments) in rapid acquisition mode, using a 2D Varex 4343RF amorphous silicon detector (2880 × 2880 pixels and 150 × 150 μm pixel size) with a sample-to-detector distance of 800 mm. During the measurement, the sample stage was placed in a Helium filled chamber to avoid air scattering. The incident wavelength of the X-rays was $\lambda = 0.1220$ Å (101.62 keV). Calibration of the experimental setup was performed using a Ni standard sample.

***In situ* X-ray total scattering experiments.** Samples were prepared in a nitrogen-filled glovebox by mixing the precursors (see ZrO_2 synthesis) in molten tri-n-octylphosphine oxide. The mixture was then transferred to a 3 mm NMR tube and sealed. The samples were measured using beamline P21.1 at DESY in Hamburg, Germany. A home-built aluminum block with an NMR tube holder and cartridge heaters were used to establish the reaction environment. The temperature was first ramped to 340 °C followed by a plateau for 2 hours with Lakeshore 336 cryogenic temperature controller. The sample stage was placed in a helium-filled chamber to avoid air scattering. The data was continuously collected in rapid

acquisition mode using a 2D Varex 4343RF amorphous silicon detector (2880 × 2880 pixels and 150 × 150 μm pixel size) with a sample-to-detector distance of 800 mm, with exposure time 2seconds. The incident wavelength of the X-rays was λ = 0.1220 Å (101.62 keV). Calibration of the experimental setup was performed using a Ni standard sample.

Analysis of x-ray total scattering data. Raw 2D data were corrected for geometrical effects and polarization, then azimuthally integrated to produce 1D scattering intensities versus the magnitude of the momentum transfer Q (where Q = 4π sinθ/λ for elastic scattering) using the program Fit2D. The program xPDFsuite with PDFgetX3 was used to perform the background subtraction, further corrections, and normalization to obtain the reduced total scattering structure function F(Q), and Fourier transformation to obtain the pair distribution function (PDF), G(r).[41,42] The refinement for each data point was carried out using Diffpy-CMI with a dual-phase fit.[43]

Small-angle X-ray scattering experiments. The SAXS experiments were performed on the SWING beamline at SOLEIL synchrotron (Saint Aubin, France). The sample to SAXS detector distances were 0.5 m (for the $ZrBr_4$ synthesis) and 3 m (for the $ZrCl_4$ synthesis). Aliquots collected at different stages of the reactions (during the heating ramp at 300°C, 320°C, 340°C and after 1, 3, 6, 9, 12, 15, 20, 25, 30, 60, 90 and 120 minutes at 340 °C). The samples were measured in a flow-through setup which enables the scattering patterns of the empty capillary, the solvent (toluene), and the solutions to be measured at exactly the same spot in the capillary. This allows the same background signals to be subtracted and to obtain the pattern on an absolute scale. Each sample were measured 10 times and the signals were then averaged. The 2D SAXS images were radially averaged using beamline-specific procedures. Then, the capillary signals were subtracted. The signal of the toluene solvent is used to obtain an absolute scale. From the isothermal compressibility of toluene, the intensity at high q is 0.0026 mm^{-1}. This was used to determine a multiplying factor that was applied to all the samples. The solvent signal was then subtracted to obtain all samples in absolute intensity (1A-B). Details of the fitting are located in SI.

Acknowledgement

J.D.R., R.P., and J.P.M. thank the University of Basel and the SNF Eccelenza funding scheme (project number: 194172). S.J.L.B. was supported by the U.S. National Science Foundation through grant DMREF-1922234. K.M.Ø.J., J.K.M., and S.R.C. are grateful to the Villum Foundation for financial support through a Villum Young Investigator grant (VKR00015416). Funding from the Danish Ministry of Higher Education and Science through the SMART Lighthouse is gratefully acknowledged. We thank DANSCATT (supported by the Danish Agency for Science and Higher Education) for support for beamtime travel. S.R.C. received funding from the European Unions Horizon 2020 research and innovation programme under the Marie Sklodowska-Curie grant agreement no. 841903. The authors acknowledge Prof. Catherine Housecroft for fruitful discussions. The total scattering experiments were performed on beamline ID15 at the European Synchrotron Radiation Facility (ESRF), Grenoble, France (proposal ch-5674). We acknowledge DESY (Hamburg, Germany), a member of the Helmholtz Association HGF, for the provision of experimental facilities. Parts of this research were carried out at PETRA III and we would like to thank Dr. Ann-Christin Dippel for assistance in using beamline P21.1. Beamtime was allocated for proposal I20200150.

Supporting Information Available

This will usually read something like: "Experimental procedures and characterization data for all new compounds.

References

(1) Lamer, V. K.; Dinegar, R. H. Theory, Production and Mechanism of Formation of Monodispersed Hydrosols. *Journal of the American Chemical Society* **1950**, *72*, 4847–

4854.

(2) Matijevic, E. Preparation and properties of uniform size colloids. *Chemistry of Materials* **1993**, *5*, 412–426.

(3) Whitehead, C. B.; Özkar, S.; Finke, R. G. LaMer's 1950 Model for Particle Formation of Instantaneous Nucleation and Diffusion-Controlled Growth: A Historical Look at the Model's Origins, Assumptions, Equations, and Underlying Sulfur Sol Formation Kinetics Data. *Chemistry of Materials* **2019**, *31*, 7116–7132.

(4) Mozaffari, S.; Li, W.; Thompson, C.; Ivanov, S.; Seifert, S.; Lee, B.; Kovarik, L.; Karim, A. M. Colloidal nanoparticle size control: experimental and kinetic modeling investigation of the ligand–metal binding role in controlling the nucleation and growth kinetics. *Nanoscale* **2017**, *9*, 13772–13785.

(5) Prins, P. T. et al. Extended Nucleation and Superfocusing in Colloidal Semiconductor Nanocrystal Synthesis. *Nano Letters* **2021**, *21*, 2487.

(6) McMurtry, B. M.; Qian, K.; Teglasi, J. K.; Swarnakar, A. K.; De Roo, J.; Owen, J. S. Continuous Nucleation and Size Dependent Growth Kinetics of Indium Phosphide Nanocrystals. *Chemistry of Materials* **2020**, *32*, 4358–4368.

(7) Campos, M. P.; De Roo, J.; Greenberg, M. W.; McMurtry, B. M.; Hendricks, M. P.; Bennett, E.; Saenz, N.; Sfeir, M. Y.; Abécassis, B.; Ghose, S. K.; Owen, J. S. Growth kinetics determine the polydispersity and size of PbS and PbSe nanocrystals. *Chemical Science* **2022**, *13*, 4555–4565.

(8) Abécassis, B.; Greenberg, M. W.; Bal, V.; McMurtry, B. M.; Campos, M. P.; Guillemeney, L.; Mahler, B.; Prevost, S.; Sharpnack, L.; Hendricks, M. P.; DeRosha, D.; Bennett, E.; Saenz, N.; Peters, B.; Owen, J. S. Persistent nucleation and size dependent attachment kinetics produce monodisperse PbS nanocrystals. *Chemical Science* **2022**, *13*, 4977–4983.

(9) Abécassis, B.; Bouet, C.; Garnero, C.; Constantin, D.; Lequeux, N.; Ithurria, S.; Dubertret, B.; Pauw, B. R.; Pontoni, D. Real-Time in Situ Probing of High-Temperature Quantum Dots Solution Synthesis. *Nano Letters* **2015**, *15*, 2620–2626.

(10) Watzky, M. A.; Finke, R. G. Transition Metal Nanocluster Formation Kinetic and Mechanistic Studies. A New Mechanism When Hydrogen Is the Reductant: Slow, Continuous Nucleation and Fast Autocatalytic Surface Growth. *Journal of the American Chemical Society* **1997**, *119*, 10382–10400.

(11) Handwerk, D. R.; Shipman, P. D.; Whitehead, C. B.; Özkar, S.; Finke, R. G. Particle Size Distributions via Mechanism-Enabled Population Balance Modeling. *The Journal of Physical Chemistry C* **2020**, *124*, 4852–4880.

(12) Habraken, W. J. E. M. et al. Ion-association complexes unite classical and non-classical theories for the biomimetic nucleation of calcium phosphate. *Nature Communications* **2013**, *4*, 1507.

(13) Baumgartner, J.; Dey, A.; Bomans, P. H. H.; Le Coadou, C.; Fratzl, P.; Sommerdijk, N. A. J. M.; Faivre, D. Nucleation and growth of magnetite from solution. *Nature Materials* **2013**, *12*, 310–314.

(14) Jeon, S. et al. Reversible disorder-order transitions in atomic crystal nucleation. *Science* **2021**, *371*, 498–503.

(15) Yang, J.; Koo, J.; Kim, S.; Jeon, S.; Choi, B. K.; Kwon, S.; Kim, J.; Kim, B. H.; Lee, W. C.; Lee, W. B.; Lee, H.; Hyeon, T.; Ercius, P.; Park, J. Amorphous-Phase-Mediated Crystallization of Ni Nanocrystals Revealed by High-Resolution Liquid-Phase Electron Microscopy. *Journal of the American Chemical Society* **2019**, *141*, 763–768.

(16) Leff, D. V.; Ohara, P. C.; Heath, J. R.; Gelbart, W. M. Thermodynamic Control of Gold Nanocrystal Size: Experiment and Theory. *The Journal of Physical Chemistry* **1995**, *99*, 7036–7041.

(17) Chen, Y.; Johnson, E.; Peng, X. Formation of Monodisperse and Shape-Controlled MnO Nanocrystals in Non-Injection Synthesis: Self-Focusing via Ripening. *Journal of the American Chemical Society* **2007**, *129*, 10937–10947.

(18) Yang, Y. A.; Wu, H.; Williams, K. R.; Cao, Y. C. Synthesis of CdSe and CdTe Nanocrystals without Precursor Injection. *Angewandte Chemie International Edition* **2005**, *44*, 6712–6715.

(19) Niederberger, M.; Cölfen, H. Oriented attachment and mesocrystals: Non-classical crystallization mechanisms based on nanoparticle assembly. *Phys. Chem. Chem. Phys.* **2006**, *8*, 3271–3287.

(20) Wang, F. D.; Richards, V. N.; Shields, S. P.; Buhro, W. E. Kinetics and Mechanisms of Aggregative Nanocrystal Growth. *Chemistry of Materials* **2014**, *26*, 5–21.

(21) Pacholski, C.; Kornowski, A.; Weller, H. Self-Assembly of ZnO: From Nanodots to Nanorods. *Angewandte Chemie International Edition* **2002**, *41*, 1188–1191.

(22) Penn, R.; Banfield, J. F. Morphology development and crystal growth in nanocrystalline aggregates under hydrothermal conditions: insights from titania. *Geochimica et Cosmochimica Acta* **1999**, *63*, 1549–1557.

(23) Penn, R. L.; Banfield, J. F. Imperfect Oriented Attachment: Dislocation Generation in Defect-Free Nanocrystals. *Science* **1998**, *281*, 969–971.

(24) Yu, J. H.; Joo, J.; Park, H. M.; Baik, S.-I.; Kim, Y. W.; Kim, S. C.; Hyeon, T. Synthesis of Quantum-Sized Cubic ZnS Nanorods by the Oriented Attachment Mechanism. *Journal of the American Chemical Society* **2005**, *127*, 5662–5670.

(25) Finney, E. E.; Finke, R. G. The Four-Step, Double-Autocatalytic Mechanism for Transition-Metal Nanocluster Nucleation, Growth, and Then Agglomeration: Metal,

Ligand, Concentration, Temperature, and Solvent Dependency Studies. *Chemistry of Materials* **2008**, *20*, 1956–1970.

(26) Zheng, H.; Smith, R. K.; Jun, Y.-w.; Kisielowski, C.; Dahmen, U.; Alivisatos, A. P. Observation of Single Colloidal Platinum Nanocrystal Growth Trajectories. *Science* **2009**, *324*, 1309–1312.

(27) Chang, H. et al. Molecular-Level Understanding of Continuous Growth from Iron-Oxo Clusters to Iron Oxide Nanoparticles. *J Am Chem Soc* **2019**, *141*, 7037–7045.

(28) Jansons, A. W.; Hutchison, J. E. Continuous Growth of Metal Oxide Nanocrystals: Enhanced Control of Nanocrystal Size and Radial Dopant Distribution. *Acs Nano* **2016**, *10*, 6942–51.

(29) Dippel, A.-C.; Jensen, K. M. O.; Tyrsted, C.; Bremholm, M.; Bojesen, E. D.; Saha, D.; Birgisson, S.; Christensen, M.; Billinge, S. J. L.; Iversen, B. B. Towards atomistic understanding of polymorphism in the solvothermal synthesis of ZrO2 nanoparticles. *Acta Crystallographica Section A* **2016**, *72*, 645–650.

(30) Tyrsted, C.; Lock, N.; Jensen, K.; Christensen, M.; Bøjesen, E.; Emerich, H.; Vaughan, G.; Billinge, S.; Iversen, B. Evolution of atomic structure during nanoparticle formation. *IUCrJ* **2014**, 165–171.

(31) Joo, J.; Yu, T.; Kim, Y. W.; Park, H. M.; Wu, F.; Zhang, J. Z.; Hyeon, T. Multigram Scale Synthesis and Characterization of Monodisperse Tetragonal Zirconia Nanocrystals. *Journal of the American Chemical Society* **2003**, *125*, 6553–6557.

(32) Pokratath, R.; Van den Eynden, D.; Cooper, S. R.; Mathiesen, J. K.; Waser, V.; Devereux, M.; Billinge, S. J. L.; Meuwly, M.; Jensen, K. M. O.; De Roo, J. Mechanistic Insight into the Precursor Chemistry of ZrO2 and HfO2 Nanocrystals; towards Size-Tunable Syntheses. *JACS Au* **2022**, *2*, 827–838.

(33) De Keukeleere, K.; Coucke, S.; De Canck, E.; Van Der Voort, P.; Delpech, F.; Coppel, Y.; Hens, Z.; Van Driessche, I.; Owen, J. S.; De Roo, J. Stabilization of Colloidal Ti, Zr, and Hf Oxide Nanocrystals by Protonated Tri-n-octylphosphine Oxide (TOPO) and Its Decomposition Products. *Chemistry of Materials* **2017**, *29*, 10233–10242.

(34) Maes, J.; Castro, N.; De Nolf, K.; Walravens, W.; Abécassis, B.; Hens, Z. Size and concentration determination of colloidal nanocrystals by small-angle X-ray scattering. *Chemistry of Materials* **2018**, *30*, 3952–3962.

(35) Bojesen, E. D.; Iversen, B. B. The chemistry of nucleation. *CrystEngComm* **2016**, *18*, 8332–8353.

(36) Zobel, M.; Neder, R. B.; Kimber, S. A. J. Universal solvent restructuring induced by colloidal nanoparticles. *Science* **2015**, *347*, 292–294.

(37) Abe, S.; Capek, R. K.; De Geyter, B.; Hens, Z. Tuning the postfocused size of colloidal nanocrystals by the reaction rate: from theory to application. *Acs Nano* **2012**, *6*, 42–53.

(38) Hendricks, M. P.; Campos, M. P.; Cleveland, G. T.; Jen-La Plante, I.; Owen, J. S. A tunable library of substituted thiourea precursors to metal sulfide nanocrystals. *Science* **2015**, *348*, 1226–1230.

(39) Owen, J. S.; Park, J.; Trudeau, P. E.; Alivisatos, A. P. Reaction chemistry and ligand exchange at cadmium-selenide nanocrystal surfaces. *Journal of the American Chemical Society* **2008**, *130*, 12279–12280.

(40) Manzer, L. E.; Deaton, J.; Sharp, P.; Schrock, R. R. *Inorganic Syntheses*; John Wiley 'I&' Sons, Inc., 2007; pp 135–140.

(41) Juhas, P.; Davis, T.; Farrow, C. L.; Billinge, S. J. L. PDFgetX3: a rapid and highly automatable program for processing powder diffraction data into total scattering pair distribution functions. *Journal of Applied Crystallography* **2013**, *46*, 560–566.

(42) Yang, X.; Juhas, P.; Farrow, C. L.; Billinge, S. J. xPDFsuite: an end-to-end software solution for high throughput pair distribution function transformation, visualization and analysis. *arXiv preprint arXiv:1402.3163* **2014**,

(43) Juhás, P.; Farrow, C. L.; Yang, X.; Knox, K. R.; Billinge, S. J. L. Complex modeling: a strategy and software program for combining multiple information sources to solve ill posed structure and nanostructure inverse problems. *Acta Crystallographica* **2015**, *71*, 562–568.

TOC Graphic

Some journals require a graphical entry for the Table of Contents. This should be laid out "print ready" so that the sizing of the text is correct.
Inside the `tocentry` environment, the font used is Helvetica 8 pt, as required by *Journal of the American Chemical Society*.
The surrounding frame is 9 cm by 3.5 cm, which is the maximum permitted for *Journal of the American Chemical Society* graphical table of content entries. The box will not resize if the content is too big: instead it will overflow the edge of the box.
This box and the associated title will always be printed on a separate page at the end of the document.